




Epidemic spreading and herd immunity in a driven non-equilibrium system of strongly-interacting atoms

Zong-Kai Liu^{1,2}, Dong-Sheng Ding^{1,2*} , Yi-Chen Yu^{1,2}, Hannes Busche³, Bao-Sen Shi^{1,2}, Guang-Can Guo^{1,2}, C. Stuart Adams⁴ and Franco Nori^{5,6,7}

Abstract

It is increasingly important to understand the spatial dynamics of epidemics. While there are numerous mathematical models of epidemics, there is a scarcity of physical systems with sufficiently well-controlled parameters to allow quantitative model testing. It is also challenging to replicate the macro non-equilibrium effects of complex models in microscopic systems. In this work, we demonstrate experimentally a physics analog of epidemic spreading using optically-driven non-equilibrium phase transitions in strongly interacting Rydberg atoms. Using multiple laser beams we can impose any desired spatial structure. The observed spatially localized phase transitions simulate the outbreak of an infectious disease in multiple locations, and the splitting of the outbreak in subregions, as well as the dynamics towards “herd immunity” and “endemic state” in different regimes. The reported results indicate that Rydberg systems are versatile enough to model complex spatial-temporal dynamics.

Keywords: Rydberg atom, Epidemic spreading, Self-organization, Non-equilibrium

1 Introduction

Self-organization and non-equilibrium dynamics of complex systems emerge not only in physics, but also in other fields such as earth science, biology, and economics [1]. In these cases, many interacting objects, such as granular media [2] and flux quanta [3, 4], can be temporally stuck in metastable states, due to local energy minima. When slowly driven towards marginal stability, these extended systems exhibit avalanches at various length scales [2–4]. On the other hand, the Rydberg atoms widely used in quantum information [5–11], combine the precision of atomic physics with strong interactions among neighboring atoms, which allows us to model constrained spatial

dynamics with emerging complexity [12–16]. Besides, the precise control of the excitation probability using narrow-band lasers [17, 18] makes Rydberg atoms an excellent candidate to study non-equilibrium physics, as instabilities of equilibrium states are ubiquitous processes occurring in a variety of driven Rydberg systems. For example, Rydberg atoms in different driven configurations exhibit many fascinating characteristics of complex systems, including aggregate formation [19], non-equilibrium phase transitions [20, 21], critical points [22], self-organized criticality [23, 24], spreading and growth dynamics [25, 26], and hydrodynamics [27]. As one of the exotic phenomena in Rydberg atoms, bistability here relates to a non-equilibrium phase transition of Rydberg atoms, which is characterized by a hysteresis loop when the parameter is scanned forward and backward [20–22, 24, 28–33]. The hysteresis loop arises as a consequence of the feedback mechanism in Rydberg atoms, which is induced by the nonlinear interaction and dissipation processes among the atoms. Specifically, in the condition of electromagnetically

* Correspondence: dds@ustc.edu.cn

¹Key Laboratory of Quantum Information, University of Science and Technology of China, Hefei, Anhui 230026, China

²Synergetic Innovation Center of Quantum Information and Quantum Physics, University of Science and Technology of China, Hefei, Anhui 230026, China
Full list of author information is available at the end of the article

induced transparency (EIT), the coupling light induces transparency in the atom towards the probe light. It is within this EIT condition that the bistable behavior occurs, driven by the dependence of probe light absorption on its own intensity, thereby establishing a feedback loop. When the intensity of the probe field is below a certain threshold, the system operates in a low-absorption state, satisfying the EIT condition. However, when the intensity surpasses this threshold, the excitation of the Rydberg atoms becomes significant, resulting in a population-dependent frequency shift in the probe light. This shift leads to the occurrence of bistability.

There is a considerable interest in simulating the outbreak of infectious diseases. The accuracy of epidemic models has been considerably improved over time [34, 35]. Besides numerical simulation, it is desirable to study and replicate the macro non-equilibrium effects of complex dynamics in microscopic atomic systems. Because the atomic system is easy to scale to a larger size and is fully controlled by the experiment parameters. Moreover, many non-equilibrium phenomena cannot be broken down into global stable states; and numerous real systems are spatially inhomogeneous, e.g., the outbreak of an infectious disease can occur in multiple locations [36]. The local change of a non-equilibrium phase would result in additional complexity that manifests as phase splitting or a new emergent phase. Consequently, the study of phase transitions in engineered spatially inhomogeneous systems can be an insightful tool to improve our understanding of non-equilibrium dynamics in extended percolating systems.

Here, we model epidemic spreading dynamics using a laser-driven thermal Rydberg gas composed of rubidium-85. We have observed the analog of typical transmission profiles for susceptible-infected-recovered (SIR) and susceptible-infected-susceptible (SIS) processes with a nonlinear recovery rate. The intensity pattern of the laser beams creates a spatially inhomogeneous Rydberg excitation rate, and thus spatial domains with different Rydberg atom densities. The experimental atomic system shows an initial exponential spread of the (microscopic) “epidemic”, until the system reaches two cases: one is analogous to “herd immunity”, which stops the spread in the SIR process; another is an “endemic state”, which is a stationary state in the SIS case. The observed phase splitting and the respective multiple hysteresis loops show a good analogy with the fact that the disease starting in one place spreads to other areas. In addition, the predicted bifurcation of the SIRS model with a nonlinear recovery process can be mapped to the multiple non-equilibrium states in Rydberg systems.

This work is organized as follows: Sect. 2 introduces the Rydberg epidemic model; Sect. 3 is long and presents our results; followed by discussions and concluding remarks.

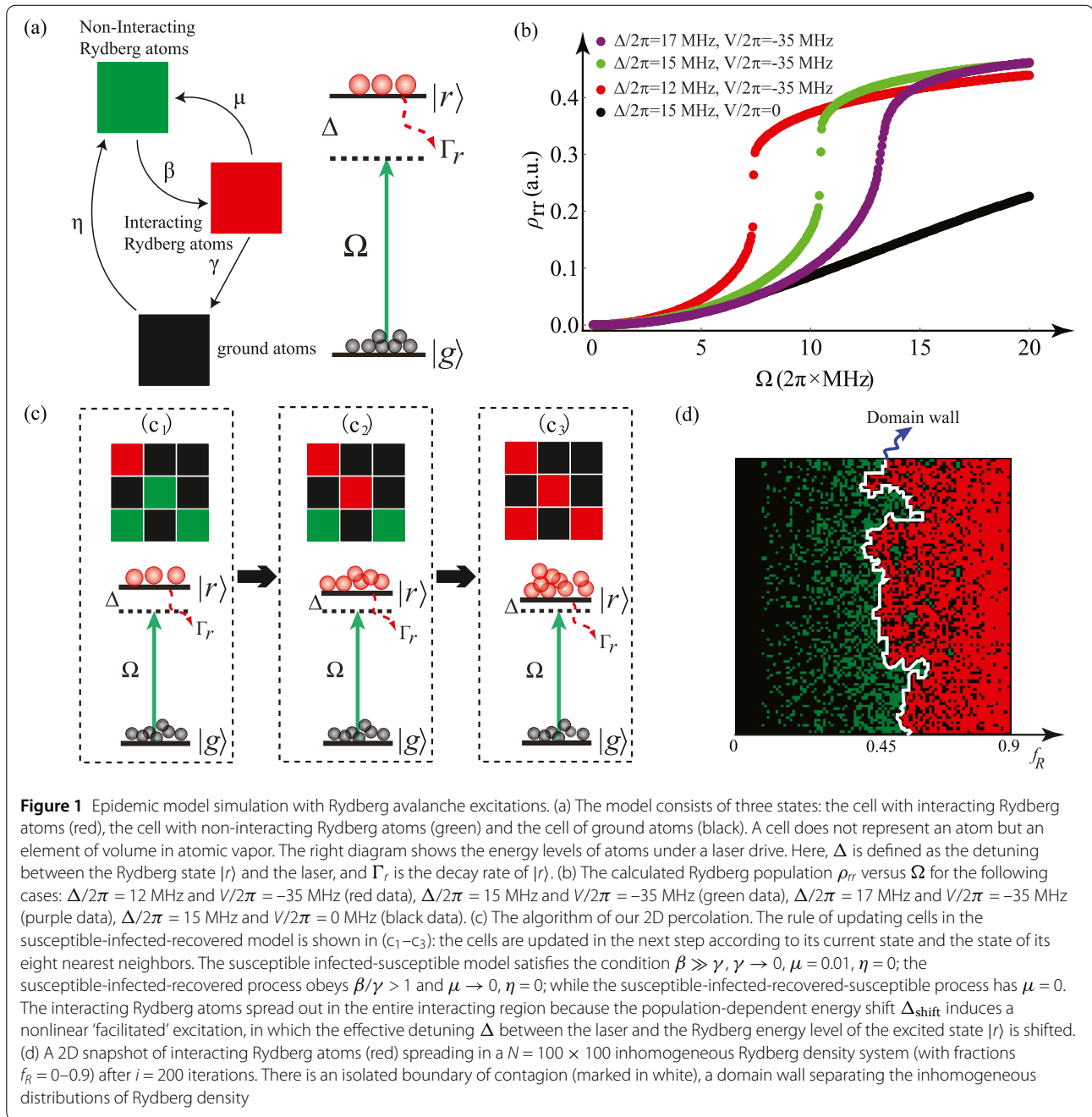
Since this work bridges two very different research areas (e.g., atomic physics and the modeling of epidemic spreading), several appendices provide background information on these models and how to relate these to our system. Moreover, considerable details about the experiments are spelled out in the [Appendix](#).

2 The Rydberg epidemic model

In order to gain insight into the spatial dynamics of Rydberg non-equilibrium phase transitions and, in particular, the spreading of the interacting phase, we build an avalanche model via the SIS, SIR, and SIRS models introduced in Refs. [36]; more details about the epidemic model and the experimental setup are shown in Appendix A and B.

The Rydberg atoms in our system can be found in one of two phases. Below a critical threshold density, interactions between Rydberg atoms are negligible; we refer to this as the ‘*non-interacting*’ (NI) phase. Above a threshold, interactions between Rydberg atoms induce a shift and broadening of the Rydberg lines; and these facilitate Rydberg excitations in adjacent regions. This triggers avalanches (cascades, chain reactions, or domino effect) of localized excitations and transitions to a ‘*strongly-interacting*’ (I) phase. The final Rydberg atomic density is controlled by the detuning Δ_c and the Rabi frequency Ω_p .

An atom in the ground state is analogous to a recovered individual. An atom in the NI phase corresponds to a susceptible individual. An atom in the I phase is analogous to an infected individual. These are schematically sketched in Fig. 1(a). The colored cells in Fig. 1(a) correspond to atoms in a micro-ensemble, in which the atoms can be either in their ground state $|g\rangle$ or their Rydberg state $|r\rangle = |47D_{3/2}\rangle$, as shown in the right diagram of Fig. 1(a). An atom in the NI phase can be excited to the I phase by a Rydberg excitation (infected, with a rate β related to the interaction strength V). Then an atom in the I phase decays to the ground state (herded, with rate γ related to the Rydberg decay Γ_r) or de-excites to the NI phase (re-susceptible, with rate μ) by the loss of Rydberg atoms. An atom in its ground state can be excited to the NI phase by a two-photon process (re-susceptible, with rate η). Specifically, the system remains susceptible until the strength of the excitation exceeds a threshold, owing to the increasing Rydberg density, controlled by the detuning Δ . Above this threshold, the system undergoes an avalanche manifested by a jump in the transmission of the probe light (the infection of the susceptible individuals). This is caused by the criticality of the Rydberg atoms in the electromagnetically induced transparency process that coherently links the ground state $|g\rangle$ with the Rydberg state $|r\rangle$. There is an inverse process where the atom becomes susceptible again from the infected state when the experiment tunes the coupling laser to lessen the influence of the $|r\rangle$ state. This pro-



cess exhibits a hysteresis that defines the bistability. Dissipation affects these coherent dynamics which is termed by γ , as a recovery probability owing to either isolation or medication.

In the experiment, the bistability occurs when the detuning Δ_c is scanned with time in a symmetric triangular wave shape, i.e., the same rate increases and decreases. As a result, the hysteresis loop of the bistability is obvious in experiment results, which is a stable solution of the nonlinear equations including the nonlinear interac-

tions between Rydberg atoms [Eq. (11) in Appendix D]. As shown in Fig. 10 of Appendix D, in the shaded area, there are three solutions for detuning Δ_c but one of the solutions is unstable. And when the detuning Δ_c is scanned within this region, the unstable solution collapsed into one of the stable solutions depending on the scan direction. This unstable solution is a result of (1) the interaction between atom and the external environment [Eq. (13) in Appendix D] and (2) feedback via the interaction among atoms.

Then, we can model the evolution of the cell by using the following time-dependent master equation with the mean-field approximation that neglects atomic motion (Doppler effect and the excitation loss induced by the atom moving in and out of the excitation area) [28, 37]:

$$\frac{d\rho_{\text{gr}}}{dt} = i\frac{\Omega}{2}(\rho_{\text{rr}} - \rho_{\text{gg}}) + i\Delta_{\text{eff}}\rho_{\text{gr}} - \frac{\Gamma_r}{2}\rho_{\text{gr}} \quad (1)$$

$$\frac{d\rho_{\text{rr}}}{dt} = -i\Omega(\rho_{\text{gr}} - \rho_{\text{rg}}) - \Gamma_r\rho_{\text{rr}} \quad (2)$$

where Δ_{eff} is the effective detuning

$$\Delta_{\text{eff}} = \Delta - V\rho_{\text{rr}} \quad (3)$$

Here, ρ_{gg} and ρ_{rr} are the populations of the ground state and Rydberg state, ρ_{gr} (ρ_{rg}) is the atomic density matrix element, Γ_r represents the decay rate of the Rydberg state, and Ω is the Rabi frequency of the excited laser. In Eq. 2 the Rydberg population operator \hat{n} is replaced by its expectation value $\text{Tr}[\rho \cdot \hat{n}] = \rho_{\text{rr}}$ in the mean-field approximation. And the anisotropy of the interaction between Rydberg atoms is neglected.

For a finite evolution time t , we calculate the Rydberg population ρ_{rr} versus Ω for different Δ , with $V/2\pi = 0$ and $V/2\pi = -35$ MHz, as shown in Fig. 1(b). From this, for increasing Ω the populations of Rydberg atoms display an avalanche process, for example, the green data in Fig. 1(b) show that ρ_{rr} undergoes a steep rise when $\Omega/2\pi \approx 10$ MHz. This process corresponds to the phase transition from the NI- to the I-phase, and the position of the jump represents the threshold. At $\Omega/2\pi \approx 10$ MHz, the cells with $\Delta/2\pi \approx 12$ MHz and $\Delta/2\pi \approx 17$ MHz are in the I-phase and NI-phase, respectively, as shown in the red and purple data in Fig. 1(b). Applying a little shift or a small change of Ω to the cells, the phase could be changed between the NI- and I-phases.

For a larger ensemble system, its evolution could be regarded as a spreading process, approximated by a discrete-state model or the cellular automaton model with the rules shown in Fig. 1(c), which corresponds to a 2D percolation model using $N(=m \times m)$ 2D cells. In this approximation, the atom ensemble is coarse-grained by N square lattices, as in Ref. [26]. The 3-D distribution of the atoms is approximated by the distribution of the atoms in 2-D square lattices. And there is more than one atom in each lattice. In the cellular automaton model, we also assume that three states evolve with the same time step. Both the time evolution and the space of our cellular automaton model are discrete. Each cell updates according to both its current state and the state of its eight nearest neighbors.

First, the cells are randomly filled with fractions f_R of Rydberg atoms. A cell is in the NI phase if $f_R < f_{R,c}$ [green cells in Fig. 1(c)], in the I phase if $f_R > f_{R,c}$ (red), or in a

depleted phase (black) without Rydberg atoms in the cell. These situations correspond to a susceptible person, an infected person, or an immune site, in the original epidemic model [36].

The procedure schematically shown in Fig. 1(c) describes the following steps: if the fraction f_R of Rydberg atoms in an arbitrary cell [red cells in Fig. 1(c₁)] exceeds the critical fraction $f_{R,c}$, and is thus in the I-phase, it increases the excitation probability of neighboring Rydberg atoms [green cells in Fig. 1(c₁)] f_R to be above $f_{R,c}$, such that the neighboring cells transition to the I phase as well in the next iteration [red cells in Fig. 1(c₂)], here the i th iteration corresponds to an iteration number for an interesting snapshot. This occurs due to level shifts Δ_{shift} by strong interactions that result in a ‘facilitated’ excitation process, which triggers an avalanche or chain reaction throughout the interaction region, corresponding to the epidemic spreading to adjacent sites; see the energy diagrams in Fig. 1(c₁–c₃). This occurs when the system’s state reverses at $\Omega/2\pi \approx 10$ MHz from the NI phase [purple data in Fig. 1(b)] to the I phase [red data in Fig. 1(b)] by changing $\Delta/2\pi = 17$ MHz to $\Delta/2\pi = 12$ MHz.

We consider the condition $\beta \gg \mu, \gamma = 0$ for the following SIS simulation, which corresponds to fast scanning either the probe intensity or Δ_c , and the system changes from the NI to the I phase. Otherwise, the system would oscillate near the critical point, and the oscillations between the phases display a bimodal distribution of transmission levels as demonstrated in Ref. [24]. This is due to the decay of the interacting Rydberg atoms, and the refilling atoms from the thermal motions, see also in Appendix. The physical boundary condition in our model is such that interacting Rydberg atoms at the edges disappear as they would move out of the excitation volume defined by the laser beams.

We have simulated the dynamics of ‘facilitated’ Rydberg excitations according to a 2D percolation model, see Fig. 1(d). After $i = 200$ iterations in a 2D inhomogeneous Rydberg density system (using initial random gradient distributions) from fractions $f_R = 0$ to $f_R = 0.9$, respectively, with $m = 100$, there is an isolated boundary edge [shown in white in Fig. 1(d)] or ‘domain wall’ that splits up the susceptible and infected regions. On the contrary, there are no obvious domain walls if using a uniform atomic density (i.e., an initial random no-gradient distribution).

Next, we use the following ordinary differential equations to model the epidemic spreading dynamics [36, 38]:

$$\frac{dS_N}{dt} = N_S - dS_N - \frac{\beta I_N S_N}{N} + \mu I_N + \eta R_N \quad (4)$$

$$\frac{dI_N}{dt} = -(v + d)I_N - \mu I_N + \frac{\beta I_N S_N}{N} - \gamma(b, I_N)I_N \quad (5)$$

$$\frac{dR_N}{dt} = -dR_N + \gamma(b, I_N)I_N - \eta R_N \quad (6)$$

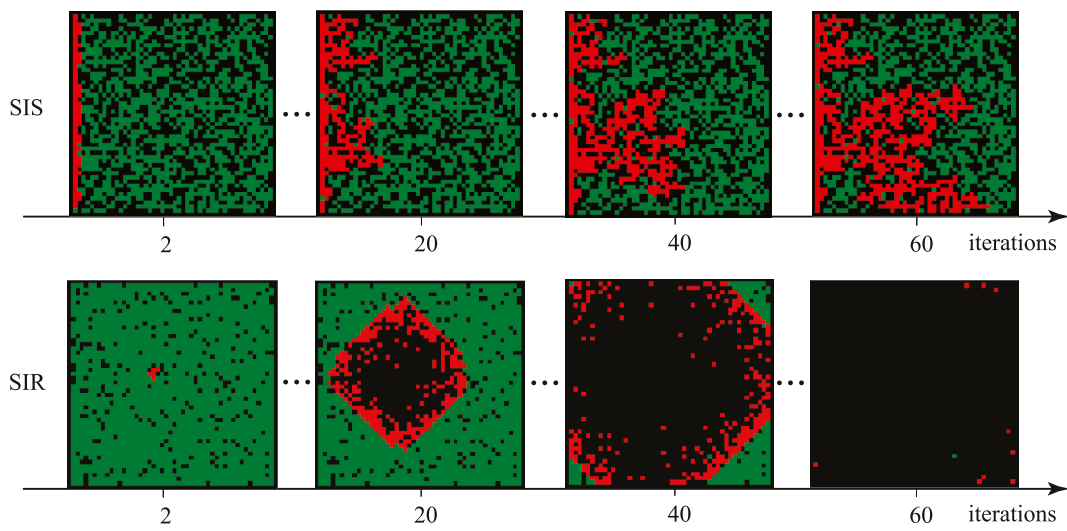


Figure 2 A 2D snapshot of interacting Rydberg atoms spreading in a 50×50 system after iterations $i = 2, 20, 40, 60$, respectively for the initial Rydberg atoms fractions $f_R = 0.9$ (SIR model) and $f_R = 0.55$ (SIS model). In the SIS model, $\mu = 0.05$, $\beta = 0.95$, and $\gamma = 0$ are used for the SIS automaton simulation. In the SIR model, the parameters $\mu = 0$, $\beta = 0.95$, and $\gamma = 0.2$ are used to demonstrate the SIR automaton simulation. Red cells correspond to the infected state I , green cells the susceptible state S , and black cells the recovered state R

where N is the initial total number of cells in the system, S_N , I_N and R_N represent the susceptible, the infected, and recovery numbers; $\gamma(b, I_N) = \gamma_0 + b(\gamma_1 - \gamma_0)/(b + I_N)$, with parameters γ_1 and γ_0 , and b represents the number of hospital beds. Also, μ , $\gamma(b, I_N)$, and β denote their corresponding rates; see more details in [Appendix](#) [see also Fig. 1(a)]; N_S is the recruitment rate of the susceptible population, d is the natural death rate, v is the per capita disease-induced death rate, and η corresponds to the immunity loss rate.

The SIS model corresponds to $\gamma = 0$ and $\eta = 0$, the SIR model has $\mu = 0$ and $\eta = 0$, while the SIRS model involves when $\mu = 0$. When considering the SIS model with $N_S = 0$, $d = 0$, and $v = 0$, the infected number $I_N(t)$ can be simplified to

$$I_N(t) = \frac{\beta + N\beta - N\mu}{\beta + e^{-(\beta + \beta I_N - \mu)t} N(\beta - \mu)} \quad (7)$$

When considering the steady-state of the SIRS model, for $N_S \neq 0$, $d \neq 0$, and $v \neq 0$, we can obtain a quadratic equation for the number I_N of infected cells:

$$AI_N^2 + BI_N + C = 0 \quad (8)$$

where, A , B , and C are the functions of b , β , d , η , γ_1 , γ_0 , v , N_S , and N . From this equation, the infected state of the system has two endemic equilibria when $B^2 - 4AC > 0$, showing a complex bifurcation dynamics for epidemic spreading [38].

3 Results

3.1 SIS and SIR modeled results in theory and experiment

In order to demonstrate the spatial evolution of the epidemic, we investigate the dynamical results of the SIS and SIR models as we change the fractions f_R of the susceptible state. We show the spreading dynamics of the infected state after different iterations $i = 2, 20, 40, 60$, for different fractions f_R .

For low fractions f_R , e.g. $f_R < 0.2$, there is almost no spread because there are not enough susceptible individuals to match close neighbor contacts, while for larger fractions f_R , i.e. $f_R = 0.9$ shown in Fig. 2 (SIR model), the infected state is more inclined to spread through all the volume. We also observe the evolution of the SIS model with $f_R = 0.55$: the infected individuals spread along local trajectories and result in a specific graph state [see the SIS model in Fig. 2].

Eventually, the final states of evolution for these two models are different. For the SIS model, the system follows a stationary state due to the cycle $I \rightarrow S \rightarrow I$; see the evolution of the system after the iteration $i = 60$ [SIS model in Fig. 2]. This stationary effect satisfies the character of “endemic state” in which the dynamic equilibrium between the susceptible and infected state is sustained for a long time. While in the SIR model, due to the recovery channel $S \rightarrow R$, most of the red and green cells change to black cells after multiple iterations [SIR model in Fig. 2], and the system finally reaches an immune state in which all infected individuals are healthy. This describes the process of “herd immunity”.

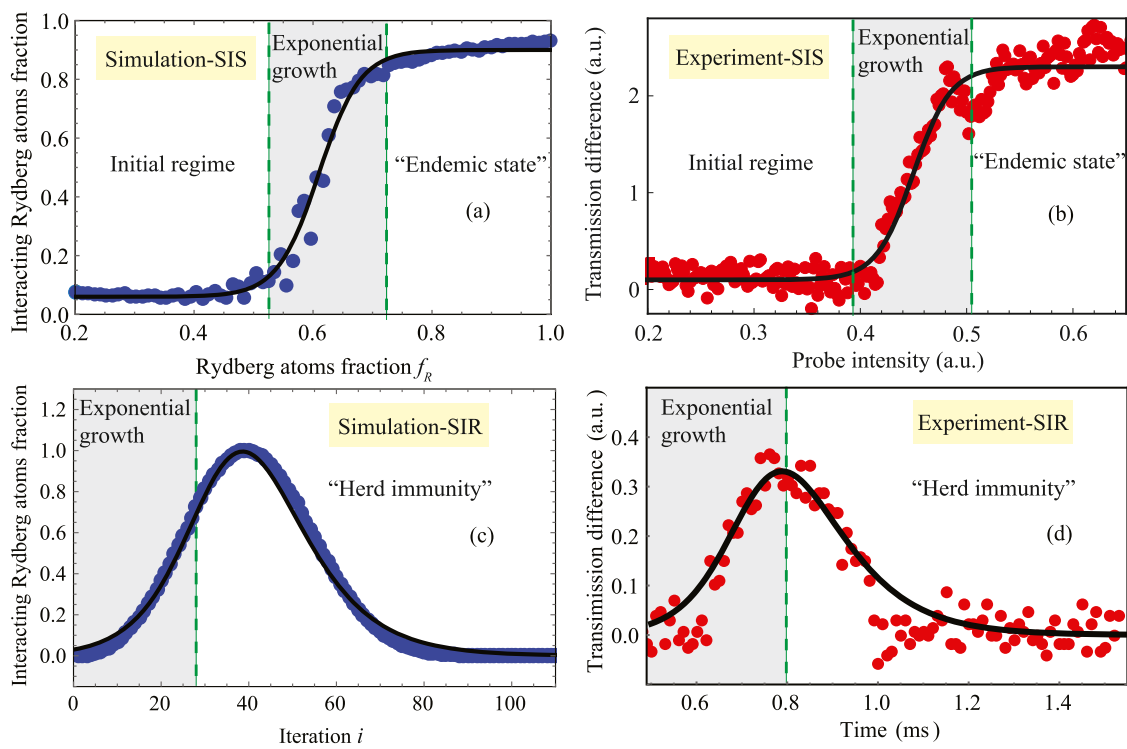


Figure 3 Epidemic nonlinear spreading (a) SIS model simulating the avalanche behavior of interacting Rydberg atoms via a 2D percolation model in an $N = 100 \times 100$ cells system. In this process, the parameters $\mu = 0.05$, $\beta = 0.95$, and $\gamma = 0$ are used for the SIS automaton simulation. Here, the plot shows the steady state versus the initial Rydberg fractions f_R . (b) Measured phase transition versus probe intensity. Here, the probe intensity is linearly modulated by a triangular wave function driving acoustic optic modulator. From the plot, it is clear that when the probe intensity is very weak, then the fraction of excited Rydberg atoms is also very small. When the probe intensity is increased by a small amount, the fraction of excited Rydberg atoms also increases by a small amount. Thus, it is not surprising to find this linear relation. These types of linear relations eventually saturate, as in the case of the Rabi frequency of two-level systems versus drive amplitude: also starting linearly, and eventually saturating. The solid lines in (a) and (b) are fit by $a/N[(t - t_0)/\tau]/N + a_0$, with parameters $a = 0.89$, $N = 10,000$, $t_0 = 0.29$, $\tau = 0.031$, $a_0 = 0.06$, $\mu = 0.05$, $\beta = 0.95$ for (a), and $a = 2.47$, $N = 10,000$, $t_0 = 0.291$, $\tau = 0.014$, $a_0 = 0.1$, $\mu = 0.1$ and $\beta = 0.9$ for (b). (c) SIR model showing a peak versus iterations in the atoms fraction. In this process, the parameters $\beta = 0.95$, and $\gamma = 0.2$ are used to demonstrate the SIR automaton simulation via a 3D percolation model in an $N = 50 \times 50 \times 50$ cells system. The initial fraction of non-interacting atoms $f_R = 0.9$ at $i = 0$. (d) The measured transmission in time without scanning laser detuning. The solid lines in (c) and (d) are fit by $a/N[(t - t_0)/\tau]/N$, according to Eqs. ((4),(5),(6)) with parameters $a = 12$, $N = 600$, $t_0 = -3.2$, $\tau = 1.15$, $\gamma = 0.25$ and $\beta = 0.4$ for (c), and $a = 2.3$, $N = 100$, $t_0 = 0.5$, $\tau = 0.011$, $\gamma = 0.18$ and $\beta = 0.34$. The interaction region considered in simulation is the nearest neighbor of each cell corresponding to the nearest-neighborhood interaction. The dynamics is divided in three regimes: initial, exponential growth, and “herd immunity” or “endemic state”. The gray areas in (a-d) are the exponential growth regions (or nonlinear outbreak) in the epidemic process

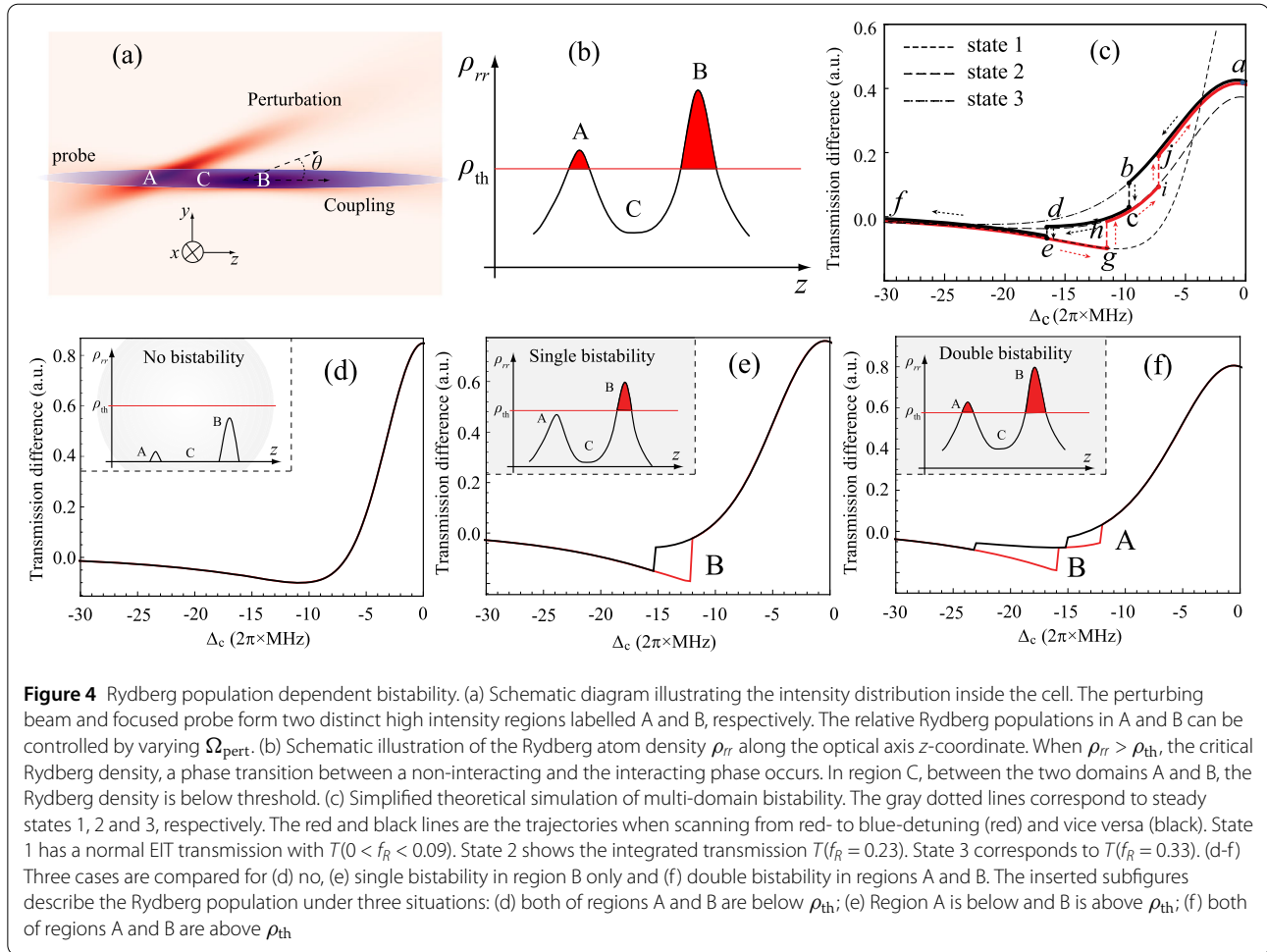
In the latter case, we record the Rydberg atoms density in the I phase after 200 iterations, and the simulated result is shown in Fig. 3(a). The interacting Rydberg fraction versus the initially filling fraction of Rydberg atoms f_R shows a critical point near a Rydberg fraction $f_{R,c} = 0.55\text{--}0.65$. In the experiment, we measure the transmission of the probe beam against the Rydberg atoms fraction by increasing the probe intensity in a two-photon electromagnetically induced transparency (EIT) scheme, see more details in Appendix.

There is a sudden jump in the probe transmission spectrum given in Fig. 3(b), which corresponds to the system transition from the NI to the I phase within the exponential growth regime. The threshold effect in the spreading of the

interacting Rydberg atoms is consistent with the nonlinear spreading characteristics in the SIS model, as predicted in Fig. 3(a). The solid curves in Fig. 3(a) and Fig. 3(b) are fit by Eq. (7), which is also almost equivalent to the tanh function.

When the system is scanned at a fast rate (see more details in Appendix), the NI and I phases tend to dynamical equilibrium, which predicts a stationary “endemic state”, a main feature of the SIS model.

When we consider the SIR process, the parameters β and μ satisfy $\beta/\gamma > 1$ and $\mu \rightarrow 0$, corresponding to the case of measuring the Rydberg excitations without scanning the laser detuning in the experiment. We have simulated the results in Fig. 3(c) with $\beta > \gamma$. The interacting Rydberg



atoms fraction first increases due to the contagion effect in the exponential regime, and then suddenly decreases because the system reaches “herd immunity” via the “infection recovery channel” in the SIR process. We have also measured the probe transmission spike near the critical point in the time domain, as shown in Fig. 3(d). The experimental Rydberg system shows the exponential spread of the (microscopic) epidemic until it reaches “herd immunity”.

3.2 Population dependent bistability

Many mixing epidemic models describe the complex dynamics (e.g., bifurcation and bistability phenomena) by modelling epidemic spreading with nonlinear incidence and recovery rates [38, 39], and antibiotic resistance [40]. For example, by considering limited medical resources, the recovery rate $\gamma(b, I_N)$ decreases with the number I_N of infected, then the infected state I can be in a metastable epidemic state, as described by Eq. (8).

In analogy to the Rydberg system, the Rydberg population ρ_{rr} decreases with a feedback from the population-dependent energy shift $V\rho_{rr}$; thus the bistability effect is

observed [20], see more details in the Appendices. The nonlinear spreading of the I phase is strongly dependent on the initial Rydberg density $f_R(t = 0)$. This reveals that one uniform spatial domain leads to one jump, and multiple spatial domains lead to multiple jumps. This corresponds to the scenario of an outbreak of an infectious disease in different locations.

To demonstrate how spatial domains with different excitation dynamics result in optical multistability, we expose part of the excitation volume to an additional probe light in the form of a single perturbing beam that intersects the probe and control beams at an angle θ , and locally enhances the Rydberg population in the region labelled A in Fig. 4(a). A second local maximum labelled B in Fig. 4(a) occurs at the focus of the probe. Thus, a spatial inhomogeneity is introduced by subjecting part of the atomic vapor to localized perturbing beams. A *dynamical phase transition* can be observed as a jump in the probe transmission as the critical Rydberg density [corresponding to the critical population ρ_{th} , shown as a horizontal red line in Fig. 4(b)] is exceeded, and an optical bistability window can be observed depending on the scan direction and

rate of change of Δ_c . The areas beyond the threshold ρ_{th} are marked in red in Fig. 4(b).

The amplitude of the perturbing field is characterized by a Rabi frequency Ω_{pert} , which can be varied independently of Ω_p . Varying Ω_{pert} can adjust the relative intensity and hence the Rydberg density in regions A and B. As the two domains are characterized by distinct Rydberg populations, they can exhibit either independent or coupled non-equilibrium dynamics depending on the size of the separation region labelled C in Fig. 4(b). The dynamics of the optical multistability along the z -axis are thus affected by the overall inhomogeneity of the Rydberg density. For any spatially varying intensity distribution, we expect distinct phases that are characterized by a spatial boundary between states of high and low population [41].

In addition to the control offered via Ω_{pert} , we can also vary both the total intensity in region A and its overlap with region B via the alignment of the perturbing beam. As expected, we find that both the intensity in region A and the separation to region B, i.e. C in Fig. 4(b) are critical. Additional perturbing fields would create more domains.

These additional domains could result in distinct optical responses. Here, we consider three distinct steady-states, 1, 2, and 3, corresponding to: no domains above threshold; one domain above threshold; and two domains above threshold, respectively. The steady-state lineshapes associated with these three steady-states are plotted as dashed lines in Fig. 4(c), see more details about calculations in Appendix. When Δ_c is scanned from red- to blue-detuning (rightwards scan direction, red line), the transmission initially evolves along the normal EIT resonance curve (steady state 1).

As Δ_c approaches resonance, ρ_{rr} increases and eventually one domain (either A or B depending on Ω_{pert}) reaches the threshold ρ_{th} , this threshold effect is also simulated by the epidemic model in the main text. At this detuning [label g in Fig. 4(c)], the system undergoes a non-equilibrium phase transition accompanied by a sudden jump in its optical transmission.

Note that the critical detuning also depends on temperature and Ω_p . Increasing Δ_c further, the system initially follows the steady-state 2 resonance curve, and then undergoes a second phase transition at point i in Fig. 4(c) as ρ_{rr} lies above threshold in both domains. In this example, the transition points g and i do not coincide due to the different local conditions in the domains A and B. By changing Ω_{pert} , g and i can be moved to coincide. Scanning Δ_c from blue- to red-detuning (leftwards scan direction, black line), the phase transitions occur at points d and b , giving rise to two hysteresis loops, see Fig. 4(c). Depending on system parameters, the two bistability loops may be either closed [Fig. 4(c)] or open. Three states with different Rydberg fractions, (for example $f_R < 0.9$, $f_R = 0.23$, and $f_R = 0.33$, respectively,) are used in the simulations.

The system transmission states $T(f_R)$ are treated as EIT transmission with different energy shifts and broadening, given by the gray lines in Fig. 4(c). The multiple discrete transmission levels arise as the transition threshold is reached for different detunings in each domain. In this process, the transmission difference decreases at the start because we use a differential scheme to obtain the amplified signal, where the probe is absorbed more than the reference via a two-photon excitation process, see details in the Appendix section.

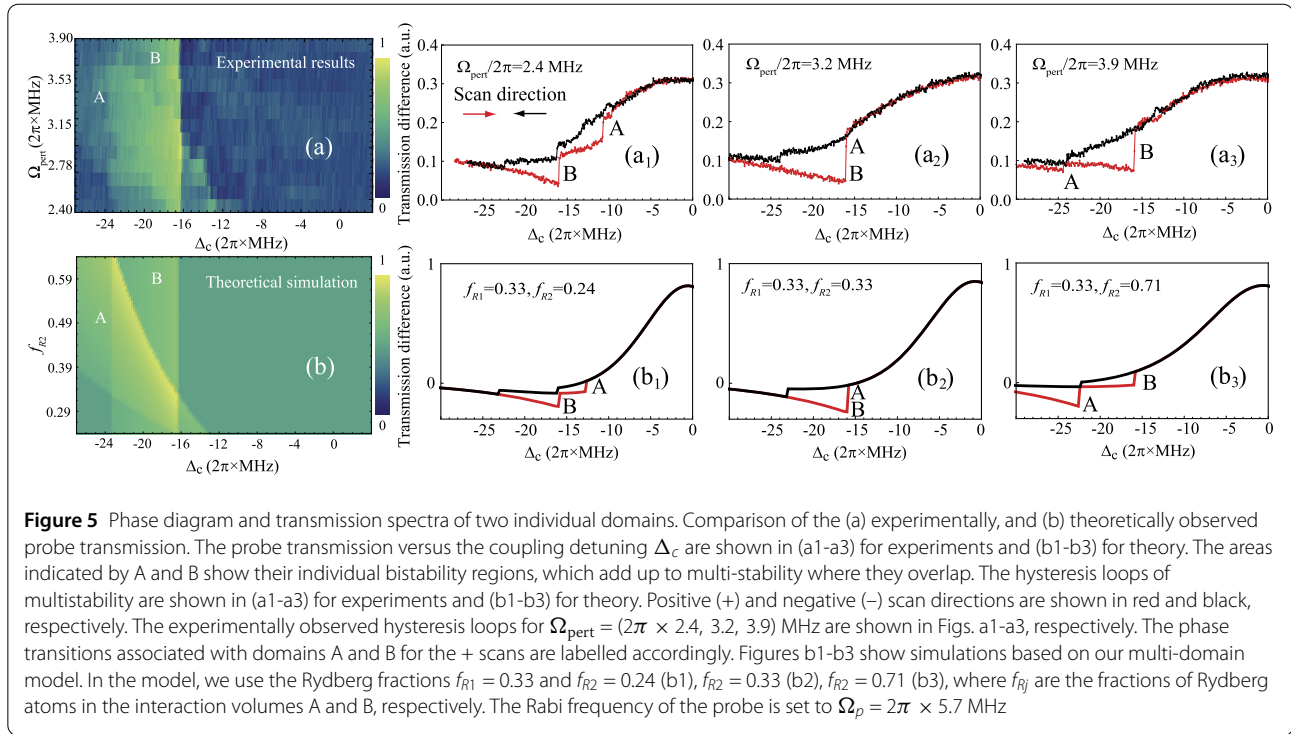
In order to highlight how the subtle difference in Rydberg population between domains A, B, and C results in optical multistability, we analyze three situations: no-, single- and double-bistability. The spatial variation of the perturbing, probe, and coupling fields leads to a spatially inhomogeneous coupling to the Rydberg state and creates an inhomogeneous Rydberg density. Once the critical Rydberg population in a given region exceeds the threshold population ρ_{th} , the state of the region would transition from the NI to the I phase, and accompanied by a jump in the probe transmission.

If the Rydberg population does not exceed the threshold population ρ_{th} in any domain, we only observe a standard EIT spectrum without any jump, as in the case in Fig. 4(d). The probe transmission spectra with positive and negative scan directions are smooth without sudden changes. If the Rydberg population in, e.g. region B, is above ρ_{th} , optical bistability occurs as in the case in Fig. 4(e). We only observe a single bistability because there is only one domain. If the Rydberg population of both domains A and B exceed ρ_{th} , but with different densities, we could observe optical multistability in the spectra, in which the two bistabilities are staggered, as shown in Fig. 4(f).

3.3 The phase diagram and transmission spectra of multistability

For the experiments, we measure the phase diagram of two independent domains by extracting the transmission difference for the $+/-$ scan directions and plotting the probe transmission versus Ω_{pert} and Δ_c in Fig. 5(a). In order to simulate the non-equilibrium behavior of the spatial domains in our phenomenological model, we consider distinct fractions f_{R1} and f_{R2} to each domain and their overall optical response. We then plot a color map of the transmission difference for the $+/-$ scan directions against f_{R2} and Δ_c by setting $f_{R1} = 0.33$, as in Fig. 5(b).

We assign distinct fractions f_{R1} and f_{R2} to each domain and combine their overall optical response. In both theory and experiments, we observe two bistable regimes and a multistable regime where the former coincide. For $\Omega_{pert} = 2\pi \times 2.4$ MHz [Fig. 5(a1)], we observe similar behaviour predicted in Fig. 4(c) or (f) with thresholds (+ scan directions) for state 2 at $\Delta_c \sim -2\pi \times 16$ MHz (transition in domain B) and state 3 at $\Delta_c \sim -2\pi \times 10$ MHz (domain A).



To demonstrate control of the phase transition point in domain A, we vary Ω_{pert} from $2\pi \times 2.4$ to $2\pi \times 3.9$ MHz. Scanning Δ_c in either direction, we obtain the experimental spectra shown in Figs. 5(a1-a3). For $\Omega_{\text{pert}} = 2\pi \times 2.4$ MHz, Fig. 5(a1), the hysteresis loops hardly overlap. For $\Omega_{\text{pert}} = 2\pi \times 3.2$ MHz, Fig. 5(a3), the transition appears at the same critical detuning as the phase transitions occur simultaneously in both domains. Comparing Fig. 5(a1-a3) and (b1-b3), the experimental and model data are in good qualitative agreement.

If we scan Δ_c more slowly for the parameters in Fig. 5(a3), the double bistability appears again because of slight population differences between domains due to fluctuations of the driving fields or vapor temperature.

3.4 Phase splitting and multiple jumps

It is insightful to increase the number of spatial domains in the experiments, and hence the number of phase jumps, by adding a few perturbing laser beams. Figures 6(a-d) show the transmission spectra with 1, 2, and 3 discrete jumps, obtained by scanning Δ_c from red- to blue-detuning.

Figure 6(a) refers to the single domain created by the probe field, showing a sudden jump in the transmission of light [gray region, where $\Delta_c/2\pi \sim -19$ MHz]. As we add the perturbing field 1 overlapping with the probe, the additional Rydberg populations are added in the subregion of the phase ①, and the jump in Fig. 6(a) is split into two jumps in Fig. 6(b), these located at the detunings $\Delta_c/2\pi \sim -19$ MHz and $\Delta_c/2\pi \sim -24$ MHz, respectively.

The local change of a non-equilibrium phase would result in additional complexity that manifests as phase splitting or a new emergent phase in Fig. 6(b). Like a phase producing another new phase, as seen by the dashed yellow circles in Fig. 6(a-b), corresponding to the locally increased infected individuals in the subregion.

Meanwhile, the phase transition is weakened, as seen from the decreased height of each jump and the susceptibility of the phase transition defined as $dT/d\Delta_c$ (dT is the transmission difference of the jump) is reduced near the transition point $\Delta_c/2\pi \sim -19$ MHz.

If a perturbing field 2 overlaps with the subregion where the population is below threshold (this region is out of the phase ①), see Fig. 6(c), a new phase ③ appears when this subregion is above the threshold by considering the effect of the additional Rydberg populations driven by the perturbing field 2. This transmission spectrum could be the result of a simple addition of the two phases, and the same effect can be seen in Fig. 5. In these two cases, as Δ_c approaches resonance, f_R increases and eventually one domain reaches the threshold $f_R^{(1)}$ at position 1 and another domain reaches the threshold $f_R^{(2)}$, the system undergoes two non-equilibrium phase transitions accompanied by two sudden jumps in the optical transmission.

Figure 6(d) shows three jumps created by both the probe and perturbing fields 1 and 2. Changing the alignment determines whether these regions overlap or are separate. Here, we extend the epidemic model to multiple spatial do-

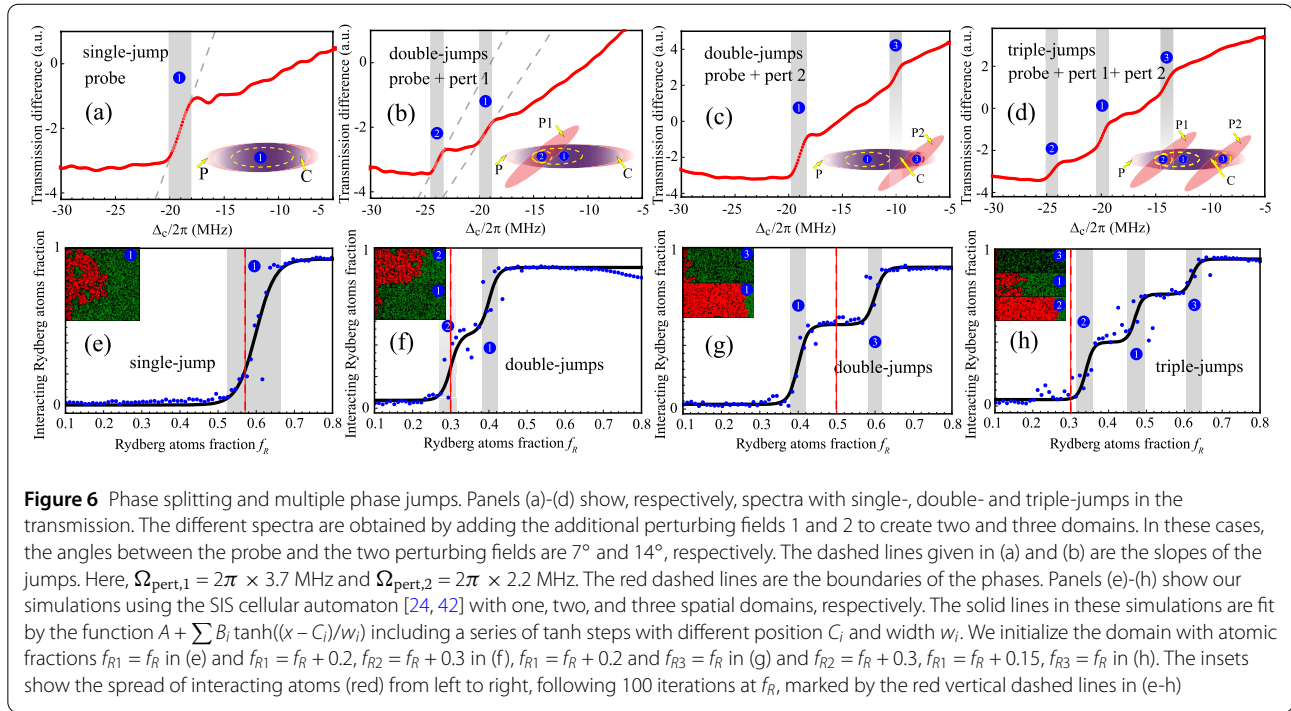


Figure 6 Phase splitting and multiple phase jumps. Panels (a)–(d) show, respectively, spectra with single-, double- and triple-jumps in the transmission. The different spectra are obtained by adding the additional perturbing fields 1 and 2 to create two and three domains. In these cases, the angles between the probe and the two perturbing fields are 7° and 14° , respectively. The dashed lines given in (a) and (b) are the slopes of the jumps. Here, $\Omega_{\text{pert},1} = 2\pi \times 3.7$ MHz and $\Omega_{\text{pert},2} = 2\pi \times 2.2$ MHz. The red dashed lines are the boundaries of the phases. Panels (e)–(h) show our simulations using the SIS cellular automaton [24, 42] with one, two, and three spatial domains, respectively. The solid lines in these simulations are fit by the function $A + \sum B_i \tanh((x - C_i)/w_i)$ including a series of tanh steps with different position C_i and width w_i . We initialize the domain with atomic fractions $f_{R1} = f_R$ in (e) and $f_{R1} = f_R + 0.2$, $f_{R2} = f_R + 0.3$ in (f), $f_{R1} = f_R + 0.2$ and $f_{R3} = f_R$ in (g) and $f_{R2} = f_R + 0.3$, $f_{R1} = f_R + 0.15$, $f_{R3} = f_R$ in (h). The insets show the spread of interacting atoms (red) from left to right, following 100 iterations at f_R , marked by the red vertical dashed lines in (e)–(h)

mains according to the 2D SIS cellular automaton. We consider one [Fig. 6(e)], two [Figs. 6(f) and 6(g)] and three regions [Fig. 6(h)] with initial random distributions but with different Rydberg fractions f_{R1} , f_{R2} and f_{R3} for each subdivision. The qualitative agreement between the predicted phase jumps, Figs. 6(e–h), and the experimental observations, Figs. 6(a–d), confirms that we can associate each jump with an individual domain.

4 Discussion

Non-equilibrium phase transitions within multi-domains often correspond to optical multistability, as demonstrated here, which is the extension of optical bistability to three or more stable output states. Before this work, multistability had been predicted and investigated in coupled atom-cavity systems [43–46] and semiconductor microcavities [47–51]. Optical bistability in Rydberg atoms has previously been studied both in theory [22, 28–31] and experiments [20, 21, 24, 32, 33]. However, optical multistability in Rydberg atoms is more challenging, and has not been explored before.

The Bloch equations with mean-field approximation is able to qualitatively simulate the multistability, because the individual Rydberg atoms interact with each other at random, in such a way that each Rydberg atom in a compartment is treated similarly and indistinguishably. More precise simulations in large-scale networks must consider the subtle differences between various states of the Rydberg atoms.

In reality, there are sudden outbreaks in the population of infections. These outbreaks are induced by the non-linearity of the epidemic spreading process. For example, as shown in Fig. 7 of Ref. [36] the bistability comes from the disconnection and re-connection of the link between susceptible individual and infected individual. Another example, in Ref. [38], demonstrates that the bistability is induced from the nonlinear recovery rate when one considers the impact of available resource of the public health system especially the number of hospital beds. In our experiment, the nonlinearity also exists in the atomic system simulating the epidemic model, induced by (1) the interaction between atoms and the external environment and (2) the spatial-structure-dependent interaction among atoms, which is concluded from the interaction term of the Hamiltonian and the master equation; see Appendix D for details. And the complexity emerges from these interactions including spatial pattern shown in Fig. 2, phase splitting (Fig. 3), bifurcations (Fig. 8) and multistability (Figs. 4 and 5). It is noted that the outbreaks in the epidemic and atomic models are both induced by the nonlinearity.

This driven non-equilibrium system of strongly-interacting quantum system can be viewed as an inanimate virus spreading simulation, providing a reference for real-world systems such as virus spreading. Furthermore, as a many-body quantum system, it may exhibit unique collective quantum effects that go beyond classical systems, such as quantum collective jumps and quantum correlations, offering a new perspective on understanding the

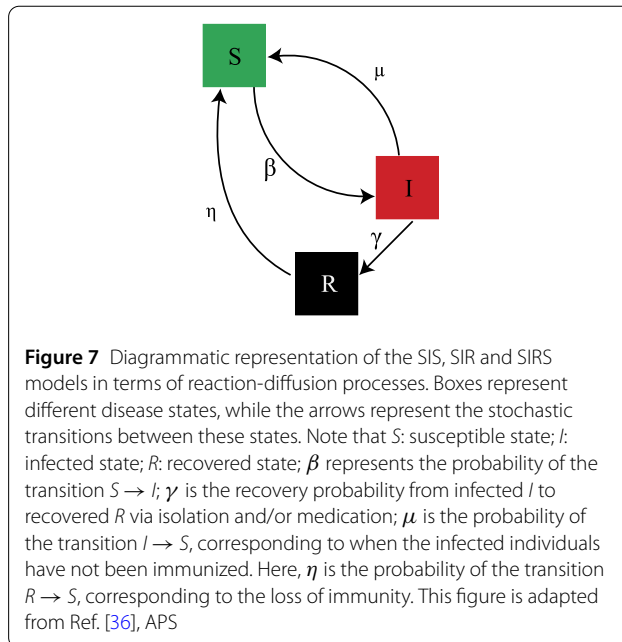
dynamics of complex quantum system. Thermal Rydberg gases offer several advantages for investigating epidemic spreading, including tunable interactions and controlled spatial structures. Unlike classical systems, such as cellular automata simulations, which struggle to model large populations [52, 53], thermal Rydberg systems can easily simulate complex behaviors by consisting of a large number of atoms, each representing a cell. Moreover, this many-body quantum system allows for precise control over experimental parameters, enabling the study of emergent behaviors, phase splitting, and unique quantum effects. The use of multiple laser beams also enables the creation of customized spatial structures, providing a highly controlled environment for studying epidemic spreading dynamics.

In summary, we have studied optically-driven multi-domain non-equilibrium dynamics in strongly interacting Rydberg atom gases. The measured hysteresis and phase jumps can be understood well and reproduced qualitatively using our epidemic model and using a mean-field master equation. The atomic model is capable of simulating the SIR and SIS models (Fig. 3) in time dynamics by adjusting the parameters of the system. Besides, in spatial domain, the initial density of infections is controlled by another laser (Fig. 4). In that case, the simulated infection is common in real life, where the infection begins as an outbreak in some areas with dense population. Finally, we show that the nonlinearity of the epidemic model (Eq. (7)) is also mimicked by the atomic system (Figs. 3 and 5), from which we deduce the universality of the self-organizing systems. But it is noted that the similarity between the atomic model and the epidemic model is come up mainly from the spreading dynamics after approximations as mentioned in section II but not from the form of the interaction in the equations.

Our results highlight the rich range of non-equilibrium phenomena that are accessible even in a relatively simple experiment and provide observational data to benchmark theoretical models of non-equilibrium dynamics under arbitrary spatial structures. Specifically, the observed dynamics of Rydberg atoms in different time and space scales can exhibit analogs of “herd immunity”, “endemic state” and the outbreak of a disease in multiple locations. The reported multi-domain-dependent exotic phases could help build a future Rydberg-based experimental analogy simulation platform for spreading in epidemiology.

Appendix A: SIS, SIR and SIRS models

Two typical epidemic spreadings can be described by the Susceptible-Infected-Susceptible (SIS), Susceptible-Infected-Recovered (SIR), and susceptible-infected-



recovered-susceptible (SIRS) models, as shown in Fig. 7. The SIS model has two simple transitions: (1) $S \rightarrow I$ happening when a susceptible individual S interacts with an infected I and becomes infected; (2) the reverse process $I \rightarrow S$ occurs when the infected individual I becomes susceptible. The SIS model does not have an immunity state, and remains in the permanent cycle $I \rightarrow S \rightarrow I$. The SIR model consists of three states: the susceptible S , infected I , and recovered states R .

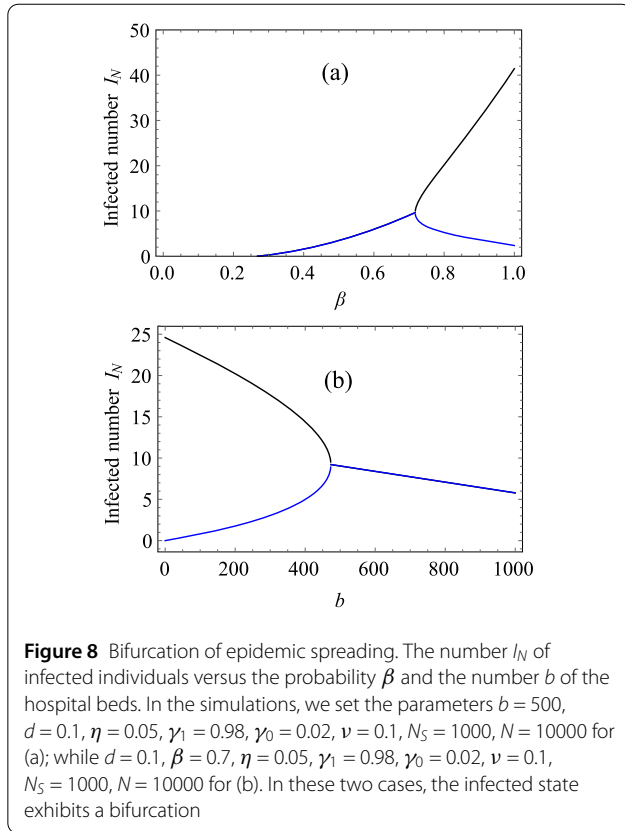
The main difference between the SIR and SIS models is that $I \rightarrow S$ is replaced by $I \rightarrow R$ in SIR model. The process $I \rightarrow R$ corresponds to the infected individual I recovering to be immune R via isolation and/or medication. In addition, the total population could not be a constant due to the non-balanced birth and death; thus we consider the natural death rate d of the states S , I and R . We also consider the disease-induced death rate ν for the state I .

In the simulation of the epidemic dynamics, the specific values of μ , β and γ play a role. A non-zero μ allows infected individuals to then become susceptible ones, lengthening the overall time of spreading. The parameter γ determines the overall time for stopping the spreading, because the recovered individuals would not be infected again.

When considering the impact of the available hospital resources, such as the number b of hospital beds, we use the simple function

$$\gamma(b, I_N) = \gamma_0 + b(\gamma_1 - \gamma_0)/(b + I_N) \quad (9)$$

to show the impact of the hospital beds. Here, the recovery rate $\gamma(b, I_N)$ decreases with the infected number I_N under



a fixed number b . If the system has real roots, as stated in the main text, two non-equilibrium epidemic states could be found.

The simulations calculating Eq. (8) are given in Fig. 8, the number of infected I_N displays a bifurcation effect against both the probability β and the number of hospital beds b . For Fig. 8(b), we find that I_N decreases with b , revealing that the disease will disappear if having enough medical resources.

Appendix B: Experimental setup

The experimental laser beams configuration is schematically shown in Fig. 4(a). We use a differential scheme in our experiments. The probe (and an identical reference beam resonant with the $|g\rangle = |5S_{1/2}, F = 3\rangle \rightarrow |e\rangle = |5P_{1/2}, F' = 2\rangle$ transition in ^{85}Rb) propagates in parallel through a heated Rb cell. The probe and reference transmission are detected on a differencing photodetector.

Aside from the addition of the perturbing field, the setup is similar to the one in Ref. [24]. Three atomic levels, a ground state $|g\rangle$, a low-lying excited state $|e\rangle$, and a Rydberg state $|r\rangle$, are driven by a probe (near-resonant with $|g\rangle \rightarrow |e\rangle$) and a coupling field (near-resonant with $|e\rangle \rightarrow |r\rangle$) with Rabi frequencies, Ω_p and Ω_c , respectively. These fields counter-propagate through a 5 cm long vapour cell

filled with ^{85}Rb atoms at $T = 60^\circ\text{C}$. The two lasers excite Rydberg atoms in a ladder-type EIT configuration [54].

The ground state atom density is $3.3 \times 10^{11} \text{ cm}^{-3}$, corresponding to a mean interatomic spacing of $0.8 \mu\text{m}$. The probe beam is focused into the cell ($1/e^2$ -waist radius $\sim 500 \mu\text{m}$) and couples the ground state $|g\rangle = |5S_{1/2}, F = 3\rangle$ to $|e\rangle = |5P_{1/2}, F' = 2\rangle$ with detuning Δ_p and Rabi frequency Ω_p . The coupling beam ($1/e^2$ -waist radius of $\sim 200 \mu\text{m}$) with detuning Δ_c is resonant with the transition from $|e\rangle$ to a Rydberg state $|r\rangle = |47D_{3/2}\rangle$ with Rabi frequency $\Omega_c \sim 2\pi \times 20 \text{ MHz}$.

By using a counter-propagating geometry, the Doppler effect induced shift becomes $\nu(w_p - w_c)/c$, where ν is the atom's velocity, and ω_p and ω_c denote the angular frequencies of the probe and coupling light. If the lifetime of $|r\rangle$ is long compared to $|e\rangle$, (i.e. the decay rates satisfy $\Gamma_r \ll \Gamma_e$, as typically the case for Rydberg states) and the probe is weak compared to the coupling field $\Omega_p \ll \Omega_c$, this corresponds to an EIT configuration where the presence of the resonant coupling field renders the ensemble transparent for the resonant probe light.

In the experiment, we fix $\Delta_p = 0$ and observe the transmission as Δ_c is scanned at different rates. The transmission of a reference field (sent through the cell in parallel and not overlapping with the coupling light) is subtracted via a pair of balanced amplified photodiodes. The photoelectric signal of the transmission difference between the probe and reference is recorded by a computer. The transmission difference is

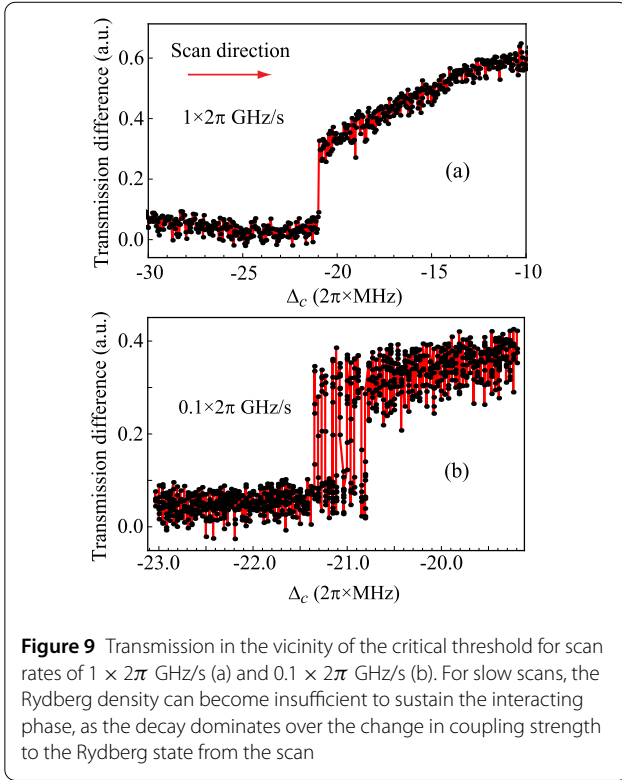
$$I_N = M(P_1 - P_2) \quad (10)$$

where M is the magnification coefficient of the detector, while $P_{1,2}$ represents the intensity of the transmitted probe and reference fields.

Appendix C: Effects of fast and slow scan of the detuning

At a low scan rate of detuning Δ_c , the spreading dynamics of the interacting phase population are affected by the finite lifetime of the Rydberg states, as well as the interacting phase, compared to the sweep speed of the coupling detuning Δ_c [Fig. 9]. The interacting Rydberg population would oscillate between $\Delta_c \approx -2\pi \times 21.3 \text{ MHz}$ and $\Delta_c \approx -2\pi \times 20.8 \text{ MHz}$, which corresponds to the case when $\beta\Delta t \sim \gamma\Delta t$ and $\mu\Delta t \rightarrow 0$ in the relatively longer time interval Δt , see Fig. 9(b).

Here, the increase in coupling strength to the Rydberg state arising from the detuning scan is low, and the interacting phase cannot be sustained because the decay plays a role in the interacting phase spreading out. This is due to



the decay of the interacting Rydberg atoms, and the refill atoms from their thermal motions; then the system exhibits instabilities and avalanches [55]. Moreover, a phase transition without oscillation appears at a fast scan rate of Δ_c , see Fig. 9(a); in this case, the spreading rate β is larger than the decay rate γ , thus $\gamma \Delta t \rightarrow 0$ or $\beta \Delta t \gg \gamma \Delta t$, $\mu \Delta t$ in a relatively short time interval Δt .

The system under the different regimes shows different non-equilibrium dynamics. Our experiments in the fast-scan regime follow the predictions of the SIS model. In the fast-scan, the interacting Rydberg atoms do not have enough time to decay, because the increased Rydberg population would supply the system with additional atoms when scanning Δ_c fast. Although the interacting Rydberg atoms are constantly excited, there are still some interacting atoms decaying into non-interacting atoms. But in a relatively long time, the system would reach a stationary state, where the interacting and the non-interacting Rydberg atoms are in dynamical equilibrium.

This process follows the predictions of the SIS model: the disease does not confer immunity and individuals can be infected over and over again, undergoing a cycle of susceptible state \rightarrow infected state \rightarrow susceptible state, which, under some conditions, can be sustained in a long time [36]. While in the slow- or no-scan regime, the system follows the predictions of the SIR model.

The system near the critical point would undergo a self-organized phase, where the lost atoms are not effectively

replenished, thus the interacting phase would transit to the no-interacting phase. For relatively long times, the interacting Rydberg atoms have enough time to be lost below the threshold ρ_{th} , and this corresponds to the process of infectious individuals recovering from the disease in the SIR model.

Appendix D: Theoretical simulation for multiple quantum jumps

Here we describe the mean-field optical Bloch equations. The Lindblad master equation is given by

$$d\rho/dt = -i[H, \rho]/\hbar + L/\hbar, \quad (11)$$

where ρ is the atomic ensemble's density matrix and $H = \sum_k H[\rho^{(k)}]$ the atom-light interaction Hamiltonian summed over all the k -th atom Hamiltonians using the rotating wave approximation. The single-atom Hamiltonian has the form:

$$H[\rho^{(k)}] = -\frac{\hbar}{2} \begin{pmatrix} 0 & \Omega_p & 0 \\ \Omega_p & -2\Delta_p & \Omega_c \\ 0 & \Omega_c & -2(\Delta_p - \Delta_c) \end{pmatrix} \quad (12)$$

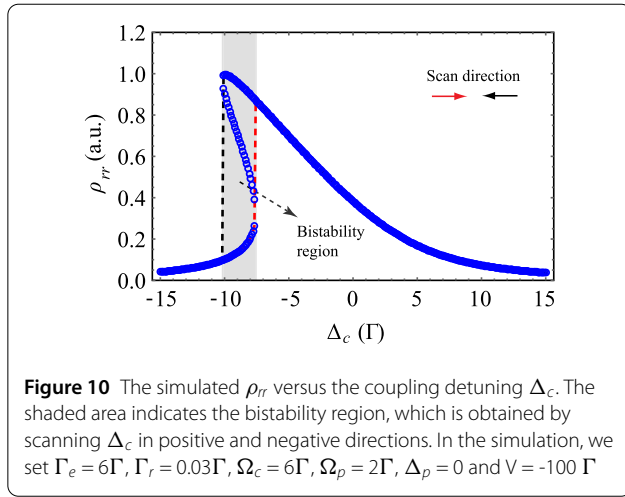
The Lindblad superoperator $L = \sum_k L[\rho^{(k)}]$ is comprised of the single-atom superoperators, where

$$L[\rho^{(k)}]/\hbar = -\frac{1}{2} \sum_m (C_m^\dagger C_m \rho + \rho C_m^\dagger C_m) + \sum_m C_m \rho C_m^\dagger \quad (13)$$

$C_1 = \sqrt{\Gamma_e} |g\rangle \langle e|$, and $C_2 = \sqrt{\Gamma_r} |e\rangle \langle r|$ are collapse operators for the decay from state $|e\rangle$ to $|g\rangle$ and from $|r\rangle$ to $|e\rangle$ with rates Γ_e and Γ_r respectively. The matrix form of the Lindbladian can be written as

$$\frac{L[\rho^{(k)}]}{\hbar} = \frac{1}{2} \begin{pmatrix} 2\Gamma_e \rho_{ee}^{(k)} & -\Gamma_e \rho_{ge}^{(k)} & -\Gamma_r \rho_{gr}^{(k)} \\ -\Gamma_e \rho_{eg}^{(k)} & -2\Gamma_e \rho_{ee}^{(k)} + 2\Gamma_r \rho_{rr}^{(k)} & -(\Gamma_e + \Gamma_r) \rho_{er}^{(k)} \\ -\Gamma_r \rho_{rg}^{(k)} & -(\Gamma_e + \Gamma_r) \rho_{re}^{(k)} & -2\Gamma_r \rho_{rr}^{(k)} \end{pmatrix} \quad (14)$$

Since we are only concerned with the steady state, i.e. $t \rightarrow \infty$, the Lindblad master equation can be solved for $d\rho/dt = 0$. Then the detuning of coupling light is modified by a mean field approximation: $\Delta_c \rightarrow \Delta_c - V\rho_{rr}$. The bistability effect of ρ_{rr} is obtained, as shown in Fig. 10. In the bistability region, the system is unstable thus resulting in a hysteresis loop, as shown by the shaded area in Fig. 10, in which there are quantum jumps [28, 56–58] in the transmission spectrum. This region is separated by the two distinct Rydberg population thresholds ρ_{th1} and ρ_{th2}



under positively and negatively scanning Δ_c , respectively ($\rho_{th1} < \rho_{th2}$ for $V < 0$).

The complex susceptibility of the EIT medium including the Doppler effect due to atomic motion is

$$\chi(\nu)d\nu = (|\mu_{ge}|^2/\epsilon_0\hbar)\rho_{eg}(\nu)d\nu, \quad (15)$$

the coherence ρ_{eg} in the density matrix is obtained by solving the master equation. It has the form

$$\rho_{eg}(\nu) = \frac{N(\nu)[\Gamma_r + 2i(\delta + \Delta_D)]}{(2\Delta_p + 2\omega_p\nu/c - i\Gamma_e)[\Gamma_r + 2i(\delta + \Delta_D) - i\Omega_{\text{eff}}^2]}. \quad (16)$$

where

$$\Delta_D = (\omega_p - \omega_c)\nu/c$$

denotes the Doppler shift experienced by an atom moving with velocity ν ,

$$\delta = \Delta_c + \Delta_p$$

is the two-photon detuning, and $N(\nu)$ is the effective atom number. Here, Ω_{eff} is defined as the average Rabi frequency of Ω_c , by considering the coupling beam size along the vapor cell. The spectra of the EIT medium are obtained from the susceptibility via

$$T(\Delta_c, \Gamma_r) \sim \exp\{-\text{Im}\left[\int kL\chi(\nu)d\nu\right]\}. \quad (17)$$

where L is the medium length and k the wavevector of the probe field. In the Doppler integration, we consider atomic velocities from $\nu = -500$ m/s to 500 m/s in order to reduce computational complexity, this velocity range covers nearly 95% of the Boltzmann-distributed atoms.

Due to the two spatial domains A and B illustrated in the inset of Fig. 4(b), we consider there are three distinct steady states, 1, 2, and 3, corresponding to: no domains above threshold; one domain above threshold; and two domains above threshold, respectively.

The steady-state lineshapes associated with these three steady-states are plotted as dashed lines in Fig. 4(c). To calculate these steady-state lineshapes, we assume that both the energy and the decay rate, Γ_r , of the Rydberg state are modified by motional averaging of interaction potentials Δ_{shift} [20, 33]. These effects could be simplify described by

$$\Delta_c \rightarrow \Delta_c + \eta_1 \cdot (f_R - f_{R,c}), \quad (18)$$

and

$$\Gamma_r \rightarrow \Gamma_r + \eta_2 \cdot (f_R - f_{R,c}), \quad (19)$$

when $f_R > f_{R,c}$, where f_R is the fraction of Rydberg atoms, and we set the critical Rydberg fraction, $f_{R,c} = 0.09$, $\eta_1 = 3$ MHz, and $\eta_2 = 50$ MHz to match the experimental results. The observation that the broadening exceeds the line shift ($\eta_2 > \eta_1$) is consistent with previous work on Rydberg-induced bistability [24, 33].

Acknowledgements

We thank for Christopher G. Wade, Kevin J. Weatherill and Igor Lesanovsky for helpful discussions on the phase boundaries and non-equilibrium dynamics.

Author contributions

D-SD conceived the idea and implemented the physical experiments with Z-KL. Z-KL, simulated the evolution of the epidemic model and calculated the SIR model. Z-KL, D-SD, Y-CY, HB, B-SS, G-CG, CSA, FN, contributed to discussions regarding the results and analysis contained in the manuscript. D-SD, B-SS, G-CG, C-SA, and FN supervised this project. All authors read and approved the final manuscript.

Funding

We acknowledge funding from National Key R&D Program of China (2017YFA0304800), NSFC funding (Grant Nos. U20A20218, 61525504, 61722510, 61435011), the Major Science and Technology Projects in Anhui Province (Grant No. 202203a13010001), the Youth Innovation Promotion Association of CAS Grant No. 2018490, EPSRC through grant agreements EP/M014398/1, EP/R002061/1, EP/L023024/1, EP/P012000/1, EP/R035482/1, EP/S015973/1, as well as, DSTL, and Durham University. The European Union's Horizon 2020 Research and Innovation Program under Grant No. 845218 (Marie Curie Fellowship to H. B.). F.N. is supported in part by: Nippon Telegraph and Telephone Corporation (NTT) Research, the Japan Science and Technology Agency (JST) [via the Quantum Leap Flagship Program (Q-LEAP), and the Moonshot R&D Grant Number JPMJMS2061], the Japan Society for the Promotion of Science (JSPS) [via the Grants-in-Aid for Scientific Research (KAKENHI) Grant No. JP20H00134], the Army Research Office (ARO) (Grant No. W911NF-18-1-0358), the Asian Office of Aerospace Research and Development (AOARD) (via Grant No. FA2386-20-1-4069), and the Foundational Questions Institute Fund (FQXi) via Grant No. FQXI-IAF19-06.

Data availability

The data are available upon reasonable request.

Declarations

Competing interests

The authors declare no competing interests.

Author details

¹Key Laboratory of Quantum Information, University of Science and Technology of China, Hefei, Anhui 230026, China. ²Synergetic Innovation Center of Quantum Information and Quantum Physics, University of Science and Technology of China, Hefei, Anhui 230026, China. ³Department of Physics, Chemistry and Pharmacy, Physics@SDU, University of Southern Denmark, 5230 Odense M, Denmark. ⁴Department of Physics, Joint Quantum Centre (JQC) Durham-Newcastle, Durham University, South Road, Durham DH1 3LE, United Kingdom. ⁵Theoretical Quantum Physics Laboratory, RIKEN Cluster for Pioneering Research, Wako-shi, Saitama 351-0198, Japan. ⁶RIKEN Center for Quantum Computing (RQC), Wako-shi, Saitama 351-0198, Japan. ⁷Physics Department, The University of Michigan, Ann Arbor, MI 48109-1040, USA.

Received: 23 July 2024 Revised: 24 October 2024

Accepted: 3 November 2024 Published online: 18 November 2024

References

- Haken H (2006) Information and self-organization: a macroscopic approach to complex systems. Springer, Berlin
- Bak P, Tang C, Wiesenfeld K (1987) Self-organized criticality: and explanation of $1/f$ noise. *Phys Rev Lett* 59:381–384
- Field S, Witt J, Nori F, Ling X (1995) Superconducting vortex avalanches. *Phys Rev Lett* 74:1206
- Olson C, Reichhardt C, Nori F (1997) Superconducting vortex avalanches, voltage bursts, and vortex plastic flow. *Phys Rev B* 56:6175
- Saffman M, Walker T, Mølmer K (2010) Quantum information with Rydberg atoms. *Rev Mod Phys* 82:2313
- Adams CS, Pritchard JD, Shaffer JP (2019) Rydberg atom quantum technologies. *J Phys B* 53:012002
- Morgado M, Whitlock S (2021) Quantum simulation and computing with Rydberg-interacting qubits. *AVS Quantum Sci* 3:023501
- Eisert J, Friesdorf M, Gogolin C (2015) Quantum many-body systems out of equilibrium. *Nat Phys* 11:124–130
- Browaeys A, Lahaye T (2020) Many-body physics with individually controlled Rydberg atoms. *Nat Phys* 16:132–142
- Bloch I, Dalibard J, Nascimbene S (2012) Quantum simulations with ultracold quantum gases. *Nat Phys* 8:267–276
- Georgescu IM, Ashhab S, Nori F (2014) Quantum simulation. *Rev Mod Phys* 86:153
- Schauß P, et al (2012) Observation of spatially ordered structures in a two-dimensional Rydberg gas. *Nature* 491:87–91
- Labuhn H, et al (2016) Tunable two-dimensional arrays of single Rydberg atoms for realizing quantum Ising models. *Nature* 534:667–684
- Bernien H, et al (2017) Probing many-body dynamics on a 51-atom quantum simulator. *Nature* 551:579–584
- de Léséleuc S, et al (2019) Observation of a symmetry-protected topological phase of interacting bosons with Rydberg atoms. *Science* 365:775–780
- Bluvstein D, et al (2021) Controlling quantum many-body dynamics in driven Rydberg atom arrays. *Science* 371:1355–1359
- Gallagher TF (2005) Rydberg atoms, vol 3. Cambridge University Press, Cambridge
- Firstenberg O, Adams CS, Hofferberth S (2016) Nonlinear quantum optics mediated by Rydberg interactions. *J Phys B* 49:152003
- Urvoy A, et al (2015) Strongly correlated growth of Rydberg aggregates in a vapor cell. *Phys Rev Lett* 114:203002
- Carr C, Ritter R, Wade C, Adams CS, Weatherill KJ (2013) Nonequilibrium phase transition in a dilute Rydberg ensemble. *Phys Rev Lett* 111:113901
- Malossi N, et al (2014) Full counting statistics and phase diagram of a dissipative Rydberg gas. *Phys Rev Lett* 113:023006
- Marcuzzi M, Levi E, Diehl S, Garrahan JP, Lesanovsky I (2014) Universal nonequilibrium properties of dissipative Rydberg gases. *Phys Rev Lett* 113:210401
- Helmrich S, et al (2020) Signatures of self-organized criticality in an ultracold atomic gas. *Nature* 577:481–486
- Ding D-S, Busche H, Shi B-S, Guo G-C, Adams CS (2020) Phase diagram and self-organizing dynamics in a thermal ensemble of strongly interacting Rydberg atoms. *Phys Rev X* 10:021023
- Pérez-Espigares C, Marcuzzi M, Gutiérrez R, Lesanovsky I (2017) Epidemic dynamics in open quantum spin systems. *Phys Rev Lett* 119:140401
- Wintermantel T, et al (2021) Epidemic growth and Griffiths effects on an emergent network of excited atoms. *Nat Commun* 12:103
- Klocke K, Wintermantel T, Lothead G, Whitlock S, Buchhold M (2021) Hydrodynamic stabilization of self-organized criticality in a driven Rydberg gas. *Phys Rev Lett* 126:123401
- Lee TE, Haeflner H, Cross M (2012) Collective quantum jumps of Rydberg atoms. *Phys Rev Lett* 108:023602
- Weimer H (2015) Variational principle for steady states of dissipative quantum many-body systems. *Phys Rev Lett* 114:040402
- Šibalić N, Wade CG, Adams CS, Weatherill KJ, Pohl T (2016) Driven-dissipative many-body systems with mixed power-law interactions: bistabilities and temperature-driven nonequilibrium phase transitions. *Phys Rev A* 94:011401
- Levi E, Gutiérrez R, Lesanovsky I (2016) Quantum non-equilibrium dynamics of Rydberg gases in the presence of dephasing noise of different strengths. *J Phys B* 49:184003
- de Melo NR, et al (2016) Intrinsic optical bistability in a strongly driven Rydberg ensemble. *Phys Rev A* 93:063863
- Weller D, Urvoy A, Rico A, Löw R, Kübler H (2016) Charge-induced optical bistability in thermal Rydberg vapor. *Phys Rev A* 94:063820
- Eubank S, et al (2004) Modelling disease outbreaks in realistic urban social networks. *Nature* 429:180–184
- Longini IM, et al (2005) Containing pandemic influenza at the source. *Science* 309:1083–1087
- Pastor-Satorras R, Castellano C, Van Mieghem P, Vespignani A (2015) Epidemic processes in complex networks. *Rev Mod Phys* 87:925
- Shammah N, Ahmed S, Lambert N, De Liberato S, Nori F (2018) Open quantum systems with local and collective incoherent processes: efficient numerical simulations using permutational invariance. *Phys Rev A* 98:063815
- Shan CH, Zhu HP (2014) Bifurcations and complex dynamics of an SIR model with the impact of the number of hospital beds. *J Differ Equ* 257:1662–1688
- Ruan SG, Wang WD (2003) Dynamical behavior of an epidemic model with a nonlinear incidence rate. *J Differ Equ* 188:135–163
- Cen XL, Feng ZL, Zheng YQ, Zhao YL (2017) Bifurcation analysis and global dynamics of a mathematical model of antibiotic resistance in hospitals. *J Math Biol* 75:1463–1485
- Inguva R, Bowden CM (1990) Spatial and temporal evolution of the first-order phase transition in intrinsic optical bistability. *Phys Rev A* 41:1670
- Drossel B, Schwabl F (1992) Self-organized critical forest-fire model. *Phys Rev Lett* 69:1629
- Kitano M, Yabuzaki T, Ogawa T (1981) Optical tristability. *Phys Rev Lett* 46:926
- Cecchi S, Giusfredi G, Petriella E, Salieri P (1982) Observation of optical tristability in sodium vapors. *Phys Rev Lett* 49:1928
- Joshi A, Xiao M (2003) Optical multistability in three-level atoms inside an optical ring cavity. *Phys Rev Lett* 91:143904
- Sheng J, Khadka U, Xiao M (2012) Realization of all-optical multistate switching in an atomic coherent medium. *Phys Rev Lett* 109:223906
- Gippius N, et al (2007) Polarization multistability of cavity polaritons. *Phys Rev Lett* 98:236401
- Paraíso T, Wouters M, Léger Y, Morier-Genoud F, Deveaud-Plédran B (2010) Multistability of a coherent spin ensemble in a semiconductor microcavity. *Nat Mater* 9:655–660
- Sarkar D, et al (2010) Polarization bistability and resultant spin rings in semiconductor microcavities. *Phys Rev Lett* 105:216402
- Cerna R, et al (2013) Ultrafast tristable spin memory of a coherent polariton gas. *Nat Commun* 4:2008
- Goblot V, et al (2019) Nonlinear polariton fluids in a flatband reveal discrete gap solitons. *Phys Rev Lett* 123:113901
- Yaakov B (2012) Biomolecular computing systems: principles, progress and potential. *Nat Rev Genet* 13:455
- Lewis G, Martyn A, Thomas GE, et al (2019) Pathways to cellular supremacy in biocomputing. *Nat Commun* 10:5250
- Mohapatra A, Jackson T, Adams C (2007) Coherent optical detection of highly excited Rydberg states using electromagnetically induced transparency. *Phys Rev Lett* 98:113003
- Klocke K, Wintermantel T, Lothead G, Whitlock S, Buchhold M (2021) Hydrodynamic stabilization of self-organized criticality in a driven Rydberg gas. *Phys Rev Lett* 126:123401
- Minganti F, Miranowicz A, Chhajlany RW, Nori F (2019) Revealing higher-order light and matter energy exchanges using quantum trajectories in ultrastrong coupling. *Phys Rev A* 100:062131

57. Minganti F, Macrì V, Settineri A, Savasta S, Nori F (2021) Dissipative state transfer and Maxwell's demon in single quantum trajectories: excitation transfer between two noninteracting qubits via unbalanced dissipation rates. *Phys Rev A* 103:052201
58. Minganti F, Macrì V, Settineri A, Savasta S, Nori F (2022) Quantum exceptional points of non-Hermitian Hamiltonians and Liouvillians: the effects of quantum jumps. *Phys Rev A* 105:023720

Publisher's Note

Springer Nature remains neutral with regard to jurisdictional claims in published maps and institutional affiliations.

Submit your manuscript to a SpringerOpen[®] journal and benefit from:

- ▶ Convenient online submission
- ▶ Rigorous peer review
- ▶ Open access: articles freely available online
- ▶ High visibility within the field
- ▶ Retaining the copyright to your article

Submit your next manuscript at ▶ [springeropen.com](https://www.springeropen.com)
